coatings

MDPI

Article

Improvement of Plasma Resistance of Anodic Aluminum-Oxide Film in Sulfuric Acid Containing Cerium(IV) Ion

Jongho So [1,2,†], Eunmi Choi [2,†], Jin-Tae Kim [2], Jae-Soo Shin [3], Je-Boem Song [2], Minjoong Kim [1,2], Chin-Wook Chung [1] and Ju-Young Yun [2,4,*]

1 Department of Electrical Engineering, Hanyang University, Seoul 04763, Korea; sjh@kriss.re.kr (J.S.); mjk@kriss.re.kr (M.K.); joykang@hanyang.ac.kr (C.-W.C.)
2 Center for Materials and Energy Measurement, Korea Research Institute of Standards and Science, Daejeon 34113, Korea; emchoi@kriss.re.kr (E.C.); kimjt@kriss.re.kr (J.-T.K.); songjb23@gmail.com (J.-B.S.)
3 Department of Advanced Materials Engineering, Daejeon University, Daejeon 34520, Korea; jsshin@dju.ac.kr
4 Division of Nano & Information Technology, University of Science and Technology, Daejeon 34113, Korea
* Correspondence: jyun@kriss.re.kr; Tel.: +82-42-868-5669
† These two authors contributed equally to this work.

Received: 5 December 2019; Accepted: 21 January 2020; Published: 23 January 2020

Abstract: The parts of equipment in a process chamber for semiconductors are protected with an anodic aluminum-oxide (AAO) film to prevent plasma corrosion. We added cerium(IV) ions to sulfuric acid in the anodizing of an AAO film to improve the plasma corrosion resistance, and confirmed that the AAO film thickness increased by up to ~20% when using 3 mM cerium(IV) ions compared with general anodizing. The α-Al_2O_3 phase increased with increasing cerium(IV) ion concentration. The breakdown voltage and etching rate improved to ~35% and 40%, respectively. The film's performance regarding the generation of contamination particles reduced by ~50%.

Keywords: plasma corrosion; plasma etch rate; anodic aluminum oxide; cerium(IV)

1. Introduction

Aluminum (Al) is often used as a material in semiconductor equipment parts because it has high ductility and excellent machinability. However, Al is easily corroded when exposed to fluorine plasma, which is used for semiconductor components and displays because it is a highly reactive metal. It is defined as contaminant particles when corroded Al particles fall on the surface.

Recently, as the environment for using semiconductor process equipment becomes increasingly severe and the difficulty of the process becomes very high, the issue of contaminant particles generated in semiconductor process equipment parts is drawing attention [1,2]. As a result, contamination particles are a major cause of decreased process yield [3–5].

To resolve this problem, plasma corrosion resistance can be improved by coating processes such as anodizing [6,7], spark-plasma sintering [8], and atmospheric plasma spraying [9]. Anodizing improves the corrosion resistance of aluminum and aluminum alloys by the growth of a porous oxide film. Anodic oxidation is an electrochemical method that is conducted in a solution, such as sulfuric acid, oxalic acid, or chromic acid [10–13]. Specially, sulfuric acid is used widely in anodizing, as it is inexpensive and yields a relatively thick anodic aluminum oxide (AAO) film that is composed of a self-sealing layer, an outer (porous) layer, and an inner (barrier) layer [14].

Rare earth elements are used in a wide range of applications, such as self-flux alloy coatings [15], aluminum alloys [16], and photocatalysts [17], because they exhibit strong chemical activities. Cerium, hafnium, and neodymium are used in various anodizing methods, such as surface preparation

before anodizing and sealing after anodizing [18–21]. In particular, many studies associated with anodizing cerium-based aluminum alloy have been reported because of its excellent corrosion inhibiting properties [19,22–24]. Saeedikhani et al. stated that cerium ions in anodizing electrolytes act as cathodic inhibitors to increase the homogeneity and growth rate of the oxide coating [19]. Additionally, M. Kending et al. proved that Ce(III) cations adsorb on the anodized aluminum pores, increasing the zeta potential and the corrosion resistance [22]. However, most studies associated with anodizing cerium-based aluminum alloys have only been evaluated from an electrochemical point of view. Therefore, the study of plasma corrosion, which is very important in the semiconductor industry, is exceedingly deficient.

In this study, cerium(IV) ions were added to a sulfuric acid electrolyte when anodizing. The characteristics of the AAO film were investigated, including the growth rate, crystallinity, and breakdown voltage with cerium(IV) ion addition. The etching rate and contamination particles were observed when the film was exposed to a $CF_4/Ar/O_2$ plasma.

2. Materials and Methods

We prepared aluminum 6061 alloy (Alfa Aesar, Haverhill, Massachusetts, USA, Table 1) with a square sample of 40 mm × 40 mm × 1 mm and a circle sample of 76 ø × 3 mm. Impurities on the aluminum-alloy surface were removed by sonication in ethanol (Duksan, Ansan, Korea, 99.8%) for 30 min. The aluminum alloy was electropolished for 120 s at 25 V, and 300 s at 20 V in 300 mL of perchloric acid (Duksan, Ansan, Korea, 70%) and 1200 mL of ethanol (Duksan, Ansan, Korea, 99.8%) to remove native surface oxide. Then, the aluminum alloy was rinsed in deionized water for 60 s.

Table 1. Al6061 alloy Chemical analysis.

Element	wt %
Al	Balance
Cu	0.278
Cr	0.130
Fe	0.143
Mg	0.962
Mn	0.015
Si	0.465
Ti	0.013
Zn	0.058

We used a constant-voltage method for anodizing. Cerium(IV) sulfate ($Ce(SO_4)_2$, Sigma Aldrich, St. Louis, Missouri, USA) (0 mM, 1 mM, 2 mM, 3 mM, and 4 mM) was added to a 1.5 M sulfuric acid (Duksan, Ansan, Korea, 95%) electrolyte, and the experiments were termed non-Ce, 1 mM-Ce, 2 mM-Ce, 3 mM-Ce, and 4 mM-Ce, respectively. During anodizing, the electrolyte was kept at 15 °C on cooling stages at 20 V for 60 min.

The thickness of the anodized sample before and after plasma etching was investigated and repeated five times per sample using an eddy-current thickness tester (ISOSCOPE FMP 10, Helmut Fisher, Sindelfingen, Germany).

The anodized sample morphology was studied by field-emission scanning electron microscopy (FE-SEM, S-4800, HITACHI, Tokyo Japan). The crystal phase was analyzed using a high-resolution X-ray diffractometer (XRD, SmartLab, RIGAKU, Tokyo, Japan) with Cu Kα radiation at 45 kV and 200 mA. The AAO film composition analysis was performed by X-ray photoelectron spectroscopy (MultiLab 2000, Thermo Scientific, Waltham, Massachusetts, USA) with Al Kα (1486.7 eV) and a total instrumental resolution of ~1 eV.

Inductively coupled plasma–reactive-ion etching (ICP-RIE) was used to study the corrosive properties of the plasma (Figure 1a). Table 2 shows the plasma-etching conditions. Additionally, in situ contamination particles that resulted from exposure to the plasma were studied using an

in-situ particle-monitoring system (ISPM, INFICON, Heidiland, Switzerland) that was mounted on a capacitive coupled-plasma(CCP) particle evaluation system (Figure 1b). A light-scattering sensor ISPM was attached to the exhaust line to measure the contamination particles based on the principles of laser light scattering [25]. In situ contaminant particles were measured when exposed to plasma for 2 h at 400 W in a 120 mTorr chamber with a gas flow, as given in Table 2. Insulator properties of the sample after exposure to plasma were measured using a breakdown-voltage measuring instrument (TOS 9200, KIKUSUI, Yokohama, Japan). We defined the breakdown voltage of the sample when 4 mA was energized with an increasing voltage to 15 V/s.

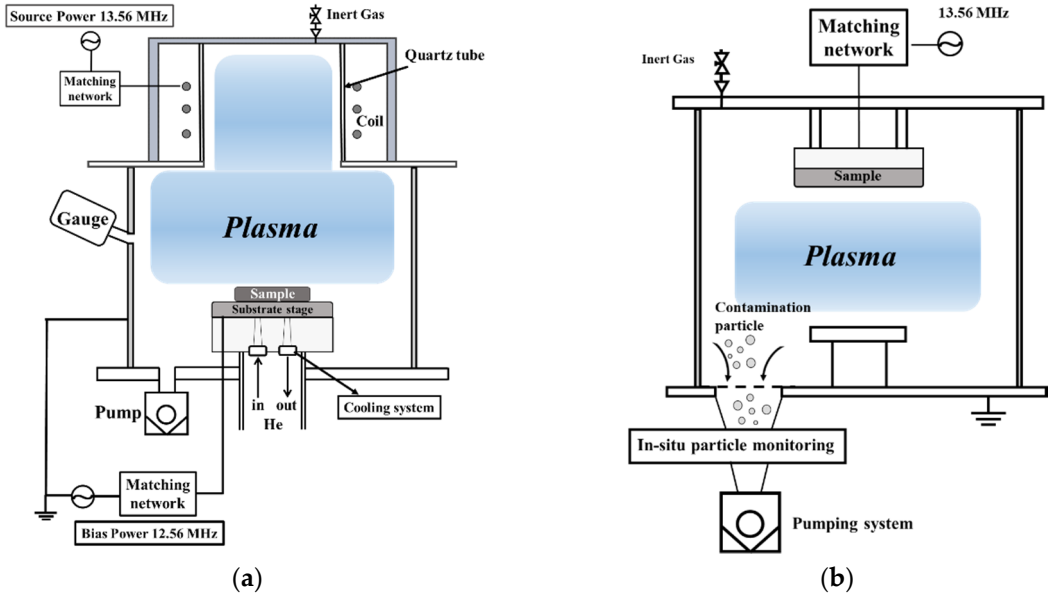

Figure 1. Schematic diagram of equipment: (**a**) ICP-RIE etching system, (**b**) CCP particle evaluation system.

Table 2. Plasma-etching conditions.

Etching Conditions		
Source power	800	W
Bias power	400	W
Gas flow (CF_4:Ar:O_2)	40:30:10	sccm
Process pressure	20	mTorr
Exposure time	60	min

3. Results

3.1. Coating Characterization

Figure 2 shows the growth rate of the AAO film and current density with cerium(IV) ion addition in sulfuric acid electrolyte. The current density during anodizing was 13.97 A/dm^2 for the non-Ce and 14.85, 15.37, 19.64, and 15.02 A/dm^2 for 1 mM-Ce, 2 mM-Ce, 3 mM-Ce, and 4 mM-Ce, respectively. The thicknesses of the oxide were 24.70, 25.90, 27.30, 30.00, and 24.90 μm for non-Ce, 1 mM-Ce, 2 mM-Ce, 3 mM-Ce, and 4 mM-Ce, respectively.

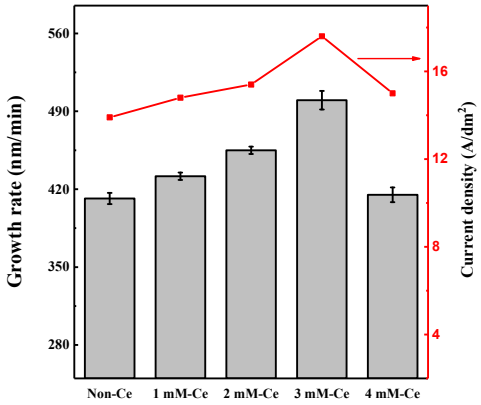

Figure 2. Growth rate of AAO film thickness and current density with change in Ce ion addition.

On the other hand, the growth rate of the AAO film increased with the addition of cerium(IV) below 3 mM, compared with the non-Ce sample. The growth rate of the AAO film was improved by ~20% for the 3 mM-Ce compared with the non-Ce. In general, the growth rate was proportional to the current density [26]. Cerium(IV) addition, with a high oxidation potential in the sulfuric acid electrolyte, increased the current density [20], which led to an increase in growth rate. However, the current density and the growth rate of the AAO film decreased to 15.02 A/dm^2 and 415 nm/min, respectively, for the 4 mM-Ce.

Cerium can be present as ions such as Ce^{3+}, Ce^{4+}, and $Ce(OH)_2^{2+}$ in sulfuric acid electrolyte, and it also can be present as salts such as $Ce(OH)_3$, Ce_2O_3, $Ce(OH)_4$, and CeO_2 [27]. It is speculated that cerium(IV) ions react with other materials in the anodizing baths, such as sulfuric acid and H_2O, when 4 mM or more cerium(IV) ions are added, forming cerium species excluding Ce^{3+}. The formed Ce species might drop the current density of anodizing solution. Therefore, we performed an additional analysis for a cerium(IV) ion addition of 3 mM or less.

Figure 3 shows the XRD patterns of the AAO film with cerium(IV) ion addition. The AAO films consisted mainly of α-Al_2O_3 and γ-Al_2O_3 [28,29]. The weak diffraction peak of Al also appeared because the Al peak originated from the substrate. The full widths at half maximum (FWHMs) of diffraction peaks α-Al_2O_3 and γ-Al_2O_3 were almost unchanged when the amount of cerium(IV) ion addition was changed.

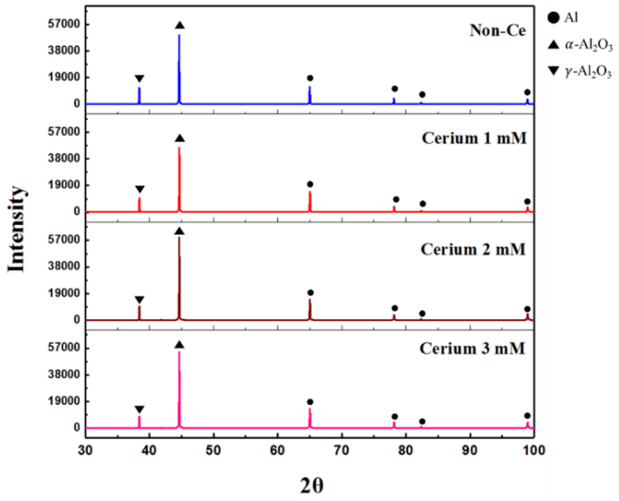

Figure 3. X-ray diffraction pattern of AAO film with change in Ce ion addition.

The α-Al_2O_3 phase is usually in a thermodynamically stable state at all temperatures, whereas the γ-Al_2O_3 phase is thermodynamically metastable. Generally, the γ-Al_2O_3 phase is more easily formed

than the α-Al_2O_3 phase, and is transformed into the α-Al_2O_3 phase at high temperature above 1300 °C. The α-Al_2O_3/γ-Al_2O_3 peak ratio according to the amount of cerium(IV) ions added to the sulfuric acid electrolyte is shown in Table 3. The ratio of the α-Al_2O_3 phase in the AAO film increased with cerium(IV) ion addition without changes in surface integrity features.

Table 3. X-ray diffraction peak ratio of α-Al_2O_3 and γ-Al_2O_3 according to Ce ion.

Electrolyte	α-Al_2O_3/γ-Al_2O_3
Non-Ce	4.14
1 mM-Ce	4.54
2 mM-Ce	6.04
3 mM-Ce	6.64

In the study of M. Kending et al., cerium ions in anodizing baths adsorbed on the surface within the pores of the AAO film and increased the zeta potential. Additionally, cerium ions were able to reversibly adsorb at the site, which could fix the proton on the surface of the AAO film [22].

The contribution of cerium ions to chemisorption during anodizing is as follows [30]:

$$-\mathrm{Al}-\mathrm{OH_2}^+ \leftrightarrows -\mathrm{Al}-\mathrm{OH} + \mathrm{H}^+$$

$$-\mathrm{Al}-\mathrm{OH} + \mathrm{Ce}^{3+} \leftrightarrows [-\mathrm{Al}-\mathrm{O}\cdots\mathrm{Ce(III)}]^2 + 2\mathrm{H}^+ \quad (1)$$

In this case, the cerium ions that are adsorbed on surface of AAO film did not exist in the Al_2O_3 crystal-lattice phase, but on the surface, and it supported α-Al_2O_3 phase nucleation [31]. Because of the reaction of the cerium ions, the α-Al_2O_3 phase increased with the addition of cerium(IV) ions.

The 3 mM-Ce was analyzed using XPS spectra to confirm the presence of cerium ions on the surface (Figure 4). However, the cerium peak did not exist in the XPS analysis results as expected. It can be expected that cerium acts as an accelerating agent, but exists on the surface below the analyzable amount in the XPS resolution.

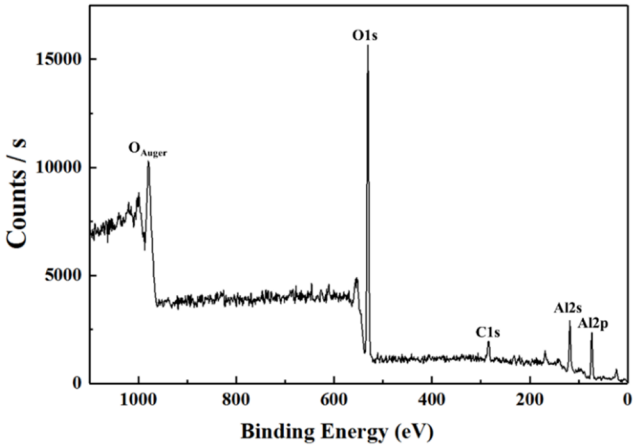

Figure 4. XPS spectrum of AAO film with the addition of 3mM Ce ions.

Figure 5 shows FE-SEM images of the AAO film surface with cerium(IV) ion addition. Pores tend to be distributed irregularly on the surface after single-step anodizing because of the field-assisted dissolution of the oxide [32]. The pores were not visible because they were covered in a self-sealing layer. The pores became visible after exposure to the CF_4/Ar/O_2 plasma because a self-sealing layer was etched by the physicochemical reaction with Ar ions and fluorine radicals (Figure 6). It was confirmed that the pore size increased gradually depending on the amount of cerium(IV) ions added (Figure 6b–d). Al transferred the stress to the cell wall region to reduce the film growth stress that

occurred during the anodizing reaction, and the transferred stress resulted in the porous structure of the AAO film due to the high plasticity of the anodic alumina [33]. When the current density increased, the AAO film growth rate increased and it led to increased AAO film growth stress. The pore diameter increased as the current density increased. When cerium(IV) ions below 3 mM were added, the applied current density was increased (Figure 2). As a result, the pore size of the AAO film was increased. It appeared that the Al-O atoms behaved differently when the cerium ions affected the formation of the Al_2O_3 phase [34].

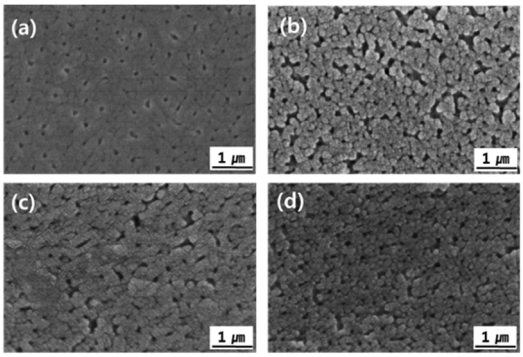

Figure 5. FE-SEM images of AAO film surfaces: (**a**) No, (**b**) 1 mM, (**c**) 2 mM, and (**d**) 3 mM Ce ion.

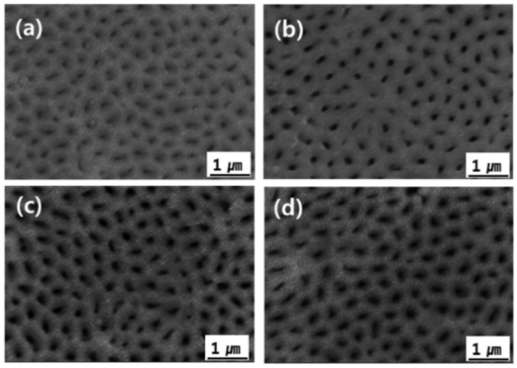

Figure 6. FE-SEM images of AAO films after exposure to $CF_4/Ar/O_2$ plasma: (**a**) No, (**b**) 1 mM, (**c**) 2 mM, and (**d**) 3 mM Ce ion.

3.2. Investigation of Plasma-Resistance Characteristics

Figure 7 shows the etching rate for the $CF_4/Ar/O_2$ plasma, which is important for the reliability of semiconductor equipment parts. Fluorine radicals generated from CF_4 promote the chemical reaction, and Ar ions that become separated from Ar gas cause physical damage [8]. Therefore, the $CF_4/Ar/O_2$ plasma caused chemical and physical damage to all components that contained the sample in the chamber.

AlF_3 is formed on the Al_2O_3 surface when Al_2O_3 reacts with fluorine plasma, and is formed with a thickness of a few nanometers by the reaction shown in Equation (2) [35]:

$$Al_2O_3 + \frac{3}{2}CF_4 \rightarrow 2AlF_3 + \frac{3}{2}CO_2 \quad (2)$$

The formed AlF_3 has a high boiling temperature of 1275 °C, which means that the AlF_3 has a high binding energy and is stable to chemical reaction [36]. Therefore, AlF_3 is physically etched only because it is chemically stable.

The etching reaction of AAO film with the $CF_4/Ar/O_2$ plasma consists of two steps. A chemical reaction occurs when Al_2O_3 reacts with the CF_4 plasma to form AlF_3 (Equation (2)), and then a physical reaction occurs in which AlF_3 reacts with the Ar plasma.

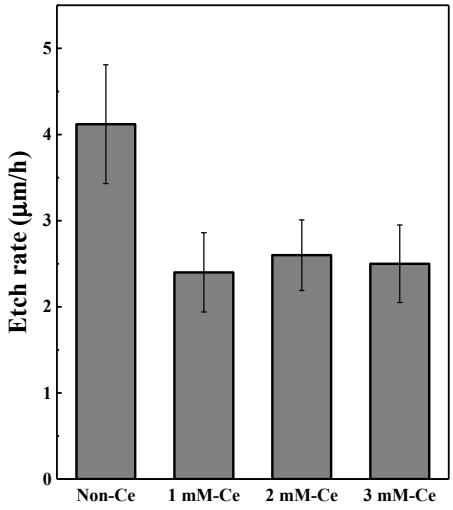

Figure 7. Etching rate of AAO film after $CF_4/Ar/O_2$ plasma exposure for 1 h.

It appears from Figure 3 and Table 3 that the AAO film with cerium(IV) ion addition had a high ratio of α-Al_2O_3 peak. It is widely known that α-Al_2O_3 is the most chemically and physically stable phase because it has a corundum structure in which oxygen anions are stacked in an ideal order on a dense plane [37]. Because of its structural characteristics, it was expected that the etching rate of the AAO film with cerium(IV) ion addition would decrease. Consequentially, we confirmed that the etching rate of the AAO film decreased by 40% with the addition of 3 mM cerium(IV) ions in a $CF_4/Ar/O_2$ plasma.

The input power increased because of an increased plasma density and a reduction in the line width during semiconductor etching. In this case, the insulation characteristic of the AAO film was important because insulator-film breakdown occurs easily because of the high voltage when a high power is applied. Figure 8a shows the measurement results of the breakdown voltage according to the amount of cerium(IV) ions added. The breakdown voltage often depends on the insulator-film thickness [38–40]. For the same time conditions, 3 mM-Ce had the highest breakdown voltage of 1.01 kV, which is ~35% higher than the non-Ce because of the highest AAO film thickness. Additionally, the breakdown voltage was measured after exposure to the $CF_4/Ar/O_2$ plasma in order to observe the insulation characteristics after plasma treatment (Figure 8b). The sample breakdown voltage with added cerium(IV) ions was still higher than in the non-Ce sample. In particular, the 3 mM-Ce (0.77 kV) that was exposed to $CF_4/Ar/O_2$ had a higher breakdown voltage than the non-Ce before (0.74 kV) and after (0.63 kV) plasma treatment. This occurred because of the thickness and dense structural characteristics of the 3 mM-Ce with a high growth rate and resistance to etching.

The generation of contamination particles is important for the reliability of the anodizing coating for parts in a process chamber for semiconductors. Figure 9 shows a number of contamination particles that were generated upon exposure to the $CF_4/Ar/O_2$ plasma. The 3 mM-Ce was compared with the non-Ce because it is an optimized process condition with the best properties.

Figure 9a shows the number of in-situ-generated contamination particles according to the exposure time to the $CF_4/Ar/O_2$ plasma. In the initial reaction, the contamination particles did not appear to be generated from the non-Ce or 3 mM-Ce. This was because of the structure of the AAO film. As mentioned previously, AAO film is composed of a self-sealing layer, an outer (porous) layer, and an inner (barrier) layer. The self-sealing layer reacts preferentially with the $CF_4/Ar/O_4$ plasma. The self-sealing layer is traditionally known as a corrosion-inhibitor layer because it has fewer reactive sites than the outer layer, with a porous structure [41]. When reacting with $CF_4/Ar/O_2$ plasma, few reaction sites exist, and the etching reaction is slow. Therefore, the number of generated contamination particles is low. After all the self-sealing layers have been etched, the outer layer and the $CF_4/Ar/O_2$ plasma react. Figure 9b shows that the amount of generated contamination particles decreased by

~50% when 3 mM cerium(IV) ions were added compared with the non-Ce case. The 3 mM-Ce sample had a high ratio of α-Al_2O_3 peak and was more physically stable than non-Ce. Hence, the sample that contained 3 mM cerium(IV) ions yielded fewer contamination particles.

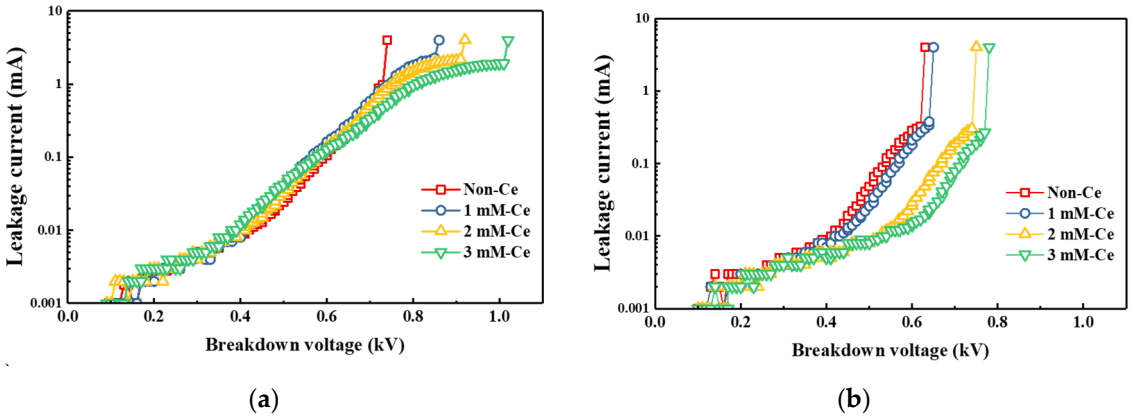

Figure 8. Breakdown voltage of AAO film with change in Ce ion addition: (**a**) before plasma treatment, (**b**) after plasma treatment.

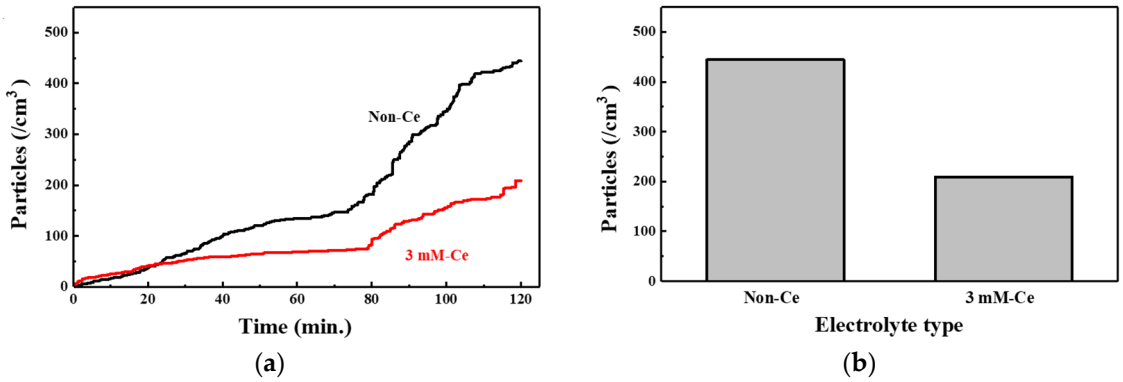

Figure 9. Generated contamination particles with exposure to $CF_4/Ar/O_2$ plasma: (**a**) in-situ generated contamination particles, (**b**) total number of generated contamination particles after 2 h.

4. Discussion

Cerium(IV) ion addition to sulfuric-acid electrolyte affected the characteristics of the AAO film, such as the thickness growth rate, breakdown voltage, and etching-gas plasma corrosion. The thickness growth rate increased by 20% and the AAO film grew at a high ratio of α-Al_2O_3 peak when 3 mM of cerium(IV) ions was added. The physical properties of the AAO film with a high ratio of α-Al_2O_3 peak improved, and led to an improvement in breakdown voltage and plasma-etching resistance of 25% and 40%, respectively. In particular, the generation of contamination particles was reduced by 50%. As a result, the AAO film with cerium(IV) ion addition has a high reliability for application as an anodic oxidation coating film in semiconductor production equipment.

Author Contributions: Conceptualization, J.S. and E.C.; formal analysis, J.-T.K., J.-S.S. and C.-W.C.; investigation, J.S.; data curation, J.-T.K., J.-B.S., M.K. and E.C.; writing—original draft preparation, J.S. and E.C.; writing—review and editing, J.S. and E.C.; supervision, J.-Y.Y. All authors have read and agreed to the published version of the manuscript.

Funding: This research was supported by the Material parts technology development program of Ministry of trade, Industry and Energy (20003660). This research was also supported by Chung-Ang University Research Grant in 2017.

Conflicts of Interest: The authors declare no conflict of interest.

References

1. Song, J.-B.; Choi, E.; Oh, S.-G.; Kim, J.-T.; Yun, J.-Y. Contamination Particle Behavior of Aerosol Deposited Y_2O_3 and YF_3 Coatings under NF_3 Plasma. *Coatings* **2019**, *9*, 310. [CrossRef]
2. Kim, D.-M.; Kim, K.-B.; Yoon, S.-Y.; Oh, Y.-S.; Kim, H.-T.; Lee, S.-M. Effects of artificial pores and purity on the erosion behaviors of polycrystalline Al_2O_3 ceramics under fluorine plasma. *J. Ceram. Soc. Jpn.* **2009**, *117*, 863–867.
3. Mun, S.Y.; Shin, K.C.; Lee, S.S.; Kwak, J.S.; Jeong, J.Y.; Jeong, Y.H. Etch defect reduction using SF_6/O_2 plasma cleaning and optimizing etching recipe in photo resist masked gate poly silicon etch process. *Jpn. J. Appl. Phys.* **2005**, *44*, 4891. [CrossRef]
4. Ito, N.; Moriya, T.; Uesugi, F.; Matsumoto, M.; Liu, S.; Kitayama, Y. Reduction of particle contamination in plasma-etching equipment by dehydration of chamber wall. *Jpn. J. Appl. Phys.* **2008**, *47*, 3630. [CrossRef]
5. Song, J.-B.; Kim, J.-T.; Oh, S.-G.; Shin, J.-S.; Chun, J.-R.; Yun, J.-Y. Effect of sealing time of anodic aluminum oxide (AAO) film for preventing plasma damage. *Sci. Adv. Mater.* **2015**, *7*, 127–132.
6. Huang, Y.; Shih, H.; Daugherty, J.; Mansfeld, F. Evaluation of the properties of anodized aluminum 6061 subjected to thermal cycling treatment using electrochemical impedance spectroscopy (EIS). *Corros. Sci.* **2009**, *51*, 2493–2501. [CrossRef]
7. Huang, Y.; Shih, H.; Huang, H.; Daugherty, J.; Wu, S.; Ramanathan, S.; Chang, C.; Mansfeld, F. Evaluation of the corrosion resistance of anodized aluminum 6061 using electrochemical impedance spectroscopy (EIS). *Corros. Sci.* **2008**, *50*, 3569–3575. [CrossRef]
8. Cao, Y.-C.; Zhao, L.; Luo, J.; Wang, K.; Zhang, B.-P.; Yokota, H.; Ito, Y.; Li, J.-F. Plasma etching behavior of Y_2O_3 ceramics: Comparative study with Al_2O_3. *Appl. Surf. Sci.* **2016**, *366*, 304–309. [CrossRef]
9. Lin, T.-K.; Wang, W.-K.; Huang, S.-Y.; Tasi, C.-T.; Wuu, D.-S. Comparison of Erosion Behavior and Particle Contamination in Mass-Production CF_4/O_2 Plasma Chambers Using Y_2O_3 and YF_3 Protective Coatings. *Nanomaterials* **2017**, *7*, 183. [CrossRef]
10. Thompson, G.; Wood, G. Porous anodic film formation on aluminium. *Nature* **1981**, *290*, 230. [CrossRef]
11. Chou, S.M.; Leidheiser, H., Jr. Wear of anodized aluminum under three-body conditions. *Ind. Eng. Chem. Prod. Res. Dev.* **1986**, *25*, 473–478. [CrossRef]
12. Kobayashi, K.; Shimizu, K. Influence of γ-Alumina on the Structure of Barrier Anodic Oxide Films on Aluminum. *J. Electrochem. Soc.* **1988**, *135*, 908–910. [CrossRef]
13. Patermarakis, G.; Moussoutzanis, K. Mathematical Models for the Anodization Conditions and Structural Features of Porous Anodic Al_2O_3 Films on Aluminum. *J. Electrochem. Soc.* **1995**, *142*, 737–743. [CrossRef]
14. Wu, Y.; Zhao, W.; Yu, J.; Xue, Q. Influence of the Self-Sealing Layer on the Corrosion of Anodic Aluminum Oxide Films. *Acs Appl. Nano Mater.* **2018**, *1*, 5142–5147. [CrossRef]
15. Wang, Y.; Liu, J.-J.; Yu, Z.-H. Effect of rare earth elements on microstructure and wear resistance of laser remelted iron alloy coatings containing metalloids. *Surf. Eng.* **1993**, *9*, 151–155. [CrossRef]
16. Mansfeld, F.; Lin, S.; Kim, K.; Shih, H. Pitting and surface modification of SIC/Al. *Corros. Sci.* **1987**, *27*, 997–1000. [CrossRef]
17. Xu, A.-W.; Gao, Y.; Liu, H.-Q. The preparation, characterization, and their photocatalytic activities of rare-earth-doped TiO_2 nanoparticles. *J. Catal.* **2002**, *207*, 151–157. [CrossRef]
18. Wang, H.; Wang, H.-W. Synergistic effect of rare earth salt and organic acid in the anodization of aluminum in phosphoric acid. *J. Mater. Sci.* **2006**, *41*, 4759–4763. [CrossRef]
19. Saeedikhani, M.; Javidi, M.; Vafakhah, S. Anodising of 2024-T3 aluminium alloy in electrolyte of sulphuric–boric–phosphoric mixed acid containing cerium salt as corrosion inhibitor. *Trans. Nonferrous Met. Soc. China* **2017**, *27*, 711–721. [CrossRef]
20. Moutarlier, V.; Gigandet, M.; Pagetti, J.; Normand, B. An electrochemical approach to the anodic oxidation of Al 2024 alloy in sulfuric acid containing inhibitors. *Surf. Coat. Technol.* **2002**, *161*, 267–274. [CrossRef]
21. Curioni, M.; Skeldon, P.; Thompson, G. Anodized anti-corrosion coatings for aluminium using rare earth metals. In *Rare Earth-Based Corrosion Inhibitors*; Elsevier: Amsterdam, The Netherlands, 2014; pp. 143–162.
22. Kendig, M.; Addison, R.; Jeanjaquet, S. Adsorption of Ce (III) on anodized aluminum. *Electrochem. Solid-State Lett.* **2000**, *3*, 266–267. [CrossRef]
23. Andreeva, R.; Stoyanova, E.; Tsanev, A.; Stoychev, D. Effect of cerium ions on the protective ability of Al_2O_3 films formed anodically during their sealing in aqueous solutions. *Bulg. Chem. Commun.* **2017**, *49*, 5–14.

24. Terada, M.; Queiroz, F.; Costenaro, H.; Olivier, M.; Costa, I.; De Melo, H. Effect of cerium (III) on the corrosion protection properties of the film formed on the AA2524-T3 alloy by hydrothermal treatments. *Eurocorr* **2016**, *2016*.
25. Miyashita, H.; Kikuchi, T.; Kawasaki, Y.; Katakura, Y.; Ohsako, N. Particle measurements in vacuum tools by in situ particle monitor. *J. Vac. Sci. Technol. A Vac. Surf. Film.* **1999**, *17*, 1066–1070. [CrossRef]
26. Lee, W.; Ji, R.; Gösele, U.; Nielsch, K. Fast fabrication of long-range ordered porous alumina membranes by hard anodization. *Nat. Mater.* **2006**, *5*, 741. [CrossRef] [PubMed]
27. Gordovskaya, I.; Hashimoto, T.; Walton, J.; Curioni, M.; Thompson, G.; Skeldon, P. Development of cerium-rich layers on anodic films formed on pure aluminium and AA7075 T6 alloy. *J. Electrochem. Soc.* **2014**, *161*, C601–C606. [CrossRef]
28. Chung, I.; Chung, C.; Su, Y. Effect of current density and concentration on microstructure and corrosion behavior of 6061 al alloy in sulfuric acid. *Surf. Coat. Technol.* **2017**, *313*, 299–306. [CrossRef]
29. Colonetti, E.; Kammer, E.H.; Junior, A.D.N. Chemically-bonded phosphate ceramics obtained from aluminum anodizing waste for use as coatings. *Ceram. Int.* **2014**, *40*, 14431–14438. [CrossRef]
30. Conde, A.; Arenas, M.; De Frutos, A.; De Damborenea, J. Effective corrosion protection of 8090 alloy by cerium conversion coatings. *Electrochim. Acta* **2008**, *53*, 7760–7768. [CrossRef]
31. Ozawa, M.; Kimura, M.; Isogai, A. Thermal stability and characterization of γ-Al_2O_3 modified with rare earths. *J. Less Common Met.* **1990**, *162*, 297–308. [CrossRef]
32. Oh, J.; Thompson, C.V. The role of electric field in pore formation during aluminum anodization. *Electrochim. Acta* **2011**, *56*, 4044–4051. [CrossRef]
33. Garcia-Vergara, S.; Iglesias-Rubianes, L.; Blanco-Pinzon, C.; Skeldon, P.; Thompson, G.; Campestrini, P. Mechanical instability and pore generation in anodic alumina. *Proc. R. Soc. A Math. Phys. Eng. Sci.* **2006**, *462*, 2345–2358. [CrossRef]
34. Kumar, K.-N.P.; Tranto, J.; Nair, B.N.; Kumar, J.; Høj, J.W.; Engell, J.E. Effect of sintering atmosphere on the pore-structure stability of cerium-doped nanostructured alumina. *Mater. Res. Bull.* **1994**, *29*, 551–558. [CrossRef]
35. Kim, D.M.; Lee, S.H.; Alexander, W.B.; Kim, K.B.; Oh, Y.S.; Lee, S.M. X-Ray Photoelectron Spectroscopy Study on the Interaction of Yttrium–Aluminum Oxide with Fluorine-Based Plasma. *J. Am. Ceram. Soc.* **2011**, *94*, 3455–3459. [CrossRef]
36. Miwa, K.; Takada, N.; Sasaki, K. Fluorination mechanisms of Al_2O_3 and Y_2O_3 surfaces irradiated by high-density CF_4/O_2 and SF_6/O_2 plasmas. *J. Vac. Sci. Technol. A Vac. Surf. Film.* **2009**, *27*, 831–835. [CrossRef]
37. Shirai, T.; Watanabe, H.; Fuji, M.; Takahashi, M. Structural properties and surface characteristics on aluminum oxide powders. *Ceramics Res. Lab* **2010**, *9*, 23–31.
38. Shin, J.-S.; Kim, M.; Song, J.-B.; Jeong, N.-G.; Kim, J.-T.; Yun, J.-Y. Fluorine Plasma Corrosion Resistance of Anodic Oxide Film Depending on Electrolyte Temperature. *Appl. Sci. Converg. Technol.* **2018**, *27*, 9–13. [CrossRef]
39. Lhymn, C.; Kosel, P.; Vaughan, R. Thickness dependence of dielectric breakdown voltage. *Thin Solid Film.* **1986**, *145*, 69–74. [CrossRef]
40. Cheng, T.-C.; Chou, C.-C. The electrical and mechanical properties of porous anodic 6061-T6 aluminum alloy oxide film. *J. Nanomater.* **2015**, *16*, 141. [CrossRef]
41. Zuo, Y.; Zhao, P.-H.; Zhao, J.-M. The influences of sealing methods on corrosion behavior of anodized aluminum alloys in NaCl solutions. *Surf. Coat. Technol.* **2003**, *166*, 237–242. [CrossRef]